Published in final edited form as:
Phys Med Biol. 2008 June 7; 53(11): 2911–2921. doi:10.1088/0031-9155/53/11/010.

Design considerations for a limited-angle, dedicated breast, TOF PET scanner

S Surti and **JS Karp**
Department of Radiology, The University of Pennsylvania, Philadelphia, PA 19104, USA

Abstract

Development of partial ring, dedicated breast PET scanners is an active area of research. Due to the limited angular coverage, generation of distortion and artifact free, fully 3D tomographic images is not possible without rotation of the detectors. With TOF information it is possible to achieve the 3D tomographic images with limited angular coverage and without detector rotation. We performed simulations for a breast scanner design with a ring diameter and axial length of 15-cm and comprising of a full (180 degree in-plane angular coverage), 2/3 (120 degree in-plane angular coverage), or ½ (90 degree in-plane angular coverage) ring detector. Our results show that as the angular coverage decreases, improved timing resolution is needed to achieve distortion-free and artifact-free images with TOF. The CRC value for small hot lesions in a partial ring scanner is similar to a full ring Non-TOF scanner. Our results indicate that a timing resolution of 600ps is needed for a 2/3 ring scanner, while a timing resolution of 300ps is needed for a ½ ring scanner. We also analyzed the ratio of lesion CRC to background pixel noise (SNR) and concluded that TOF improves the SNR values of the partial ring scanner, and helps to compensate for the loss in sensitivity due to reduced geometric sensitivity in a limited angle coverage PET scanner. In particular, it is possible to maintain similar SNR characteristic in a 2/3 ring scanner with a timing resolution of 300ps as in a full ring Non-TOF scanner.

1. Introduction

In recent years, dedicated partial ring PET devices (PEM, positron emission mammography) have been developed for use in breast imaging. Based upon our discussions with clinicians, there are two primary reasons why partial ring, as opposed to full ring, dedicated breast PET scanners are advantageous: they provide the ability to perform needle biopsy while a patient is in the scanner, and the ability to acquire the PET image in conjunction with a mammography unit placed orthogonal to the PET detectors. These dedicated breast scanners use a variety of detector configurations and scintillators arranged in close proximity to the patient, which leads to a higher sensitivity than clinical PET scanners and reduced attenuation of photons traveling through the patient chest wall (Thompson et al., 1994, Thompson et al., 1995, Doshi et al., 2000, Moses et al., 1995, Weinberg et al., 1996, Raylman et al., 2000, Raylman et al., 2001, Raylman et al., 2002, Raylman et al., 2003). The resolution of most of these scanners is in the range of 2-4-mm, with an emphasis on spatial resolution at the expense of sensitivity (short crystals) (Thompson et al., 1994, Thompson et al., 1995, Weinberg et al., 1996, Raylman et al., 2000). More recently proposed scanner designs overcome some of these limitations by utilizing detectors capable of about 1-mm spatial resolution, high sensitivity (20-mm long LSO scintillators), and depth-of-interaction (DOI) measurement capability (Levin et al., 2006, Yang et al., 2006). The DOI capability is needed in order to maintain the high spatial resolution throughout the field-of-view (FOV) of a small diameter scanner using long crystals for high

---

E-mail: surti@mail.med.upenn.edu and joelkarp@mail.med.upenn.edu.

sensitivity. However, none of these dedicated breast PET scanners produce a fully 3D reconstructed tomographic image that is very beneficial for detecting small tumors. The reason for this is the limited angle coverage of the imaging plane due to a partial detector ring, leading to an incomplete sampling of the polar angles and producing artifacts in image reconstruction (Townsend et al., 1980). As a result, focal plane tomographic techniques (Muehllehner et al., 1976) are used to produce 2D images in several parallel planes. As pointed out by others (Moses and Qi, 2003), the resultant images in these situations have a broad background, leading to reduced lesion contrast compared to a full 3D tomographic reconstruction.

In the last few years, good timing resolution achieved by scintillators such as lutetium and lutetium-yttrium oxy-orthosilicate (LSO/LYSO) and lanthanum bromide ($LaBr_3$) has re-invigorated interest in TOF PET imaging for clinical scanners that can lead to improved image quality (Conti et al., 2005, Karp et al., 2005, Surti et al., 2007). TOF PET will contribute limited image quality gains in dedicated breast scanners due to the small object size. However, as shown recently the number of angular views necessary for an artifact-free image reconstruction is reduced as timing resolution improves (Vandenberghe et al., 2006, Vandenberghe and Lemahieu, 2007). As a result, we have investigated the performance of a limited angle, but TOF-capable, breast scanner to determine whether it is possible to achieve artifact-free tomographic images for studies focused on detection and quantification of lesion in the breast. Specifically, we first study the impact of scanner spatial resolution in achieving high contrast recovery for small, low uptake lesions in a breast imaging situation. For TOF imaging capability we then study the impact of timing resolution as a function of angular coverage on achieving artifact-free images with high contrast recovery values for small, hot lesions. Finally, a simple SNR metric is used to study the trade-off in sensitivity achieved due to reduced partial angular coverage and improved timing resolution. For this study, we restrict our partial ring geometry so that only two PET detectors placed directly opposite each other are used in coincidence.

2. Methods

We performed Monte Carlo simulations for a breast scanner design in order to understand the benefit of TOF in reconstruction of limited angle PET data. The Monte Carlo simulation is based on an EGS4 simulations package which models annihilation photon emission and transmission (with attenuation and scatter) through a geometric phantom, tracks their subsequent passage through a scintillation detector configuration, models the detector light response and point spread function as well as timing resolution, and outputs a list-mode data set where each event is tagged as scattered (in the phantom) or true (unscattered) event (Adam and Watson, 1999, Surti et al., 2004, Surti et al., 2006). In this work we reconstructed only the true coincidences. The simulated scanner had a ring diameter of 15-cm and axial length of about 15-cm. Three different LSO crystal sizes were simulated for the detector: 1×1×10-mm^3, 2×2×10-mm^3, and 3×3×10-mm^3. The simulated phantoms were a 10-cm diameter by 8-cm long and a 6-cm diameter by 8-cm long cylinder, each containing three 5-mm diameter hot spheres with 8:1 uptake with respect to background (at {x,y} coordinates of {0,0}, {3,0}, and {0,−3) cm in the 10-cm diameter cylinder and at {x,y} coordinates of {0,0}, {1.8,0}, and {0, −1.8) cm in the 6-cm diameter cylinder), and one cold sphere (at {x,y} coordinates of {0,3} cm in the 10-cm diameter cylinder and at {x,y} coordinates of {0,1.8} in the 6-cm diameter cylinder). The scan times were calculated by assuming a 15-mCi ^{18}F-FDG injection followed by a 1 hour uptake period leading to an ^{18}F-FDG concentration of 0.0975-μCi/cc in the breast (representative of the average radiotracer concentration in normal breast tissue (Zasadny and Wahl, 1993)).

Image reconstruction was first performed using data from a full scanner ring (complete 180 degree in-plane angular coverage). For partial ring geometries, data from the full scanner ring simulation were gated to throw away those events not lying within the angular coverage region. In this way image reconstruction was also performed for a two-third scanner ring (120 degree in-plane angular coverage) and a half scanner ring (90 degree in-plane angular coverage) (Figure 1). For image reconstruction we used a 3D list-mode iterative reconstruction algorithm using chronologically ordered sub-sets. This algorithm uses a Gaussian TOF kernel for TOF reconstructions. Using a relaxed OSEM update equation (i.e., $\lambda=1$) with 33 subsets, we find that we can use 3–6 iterations of the reconstruction algorithm, depending upon the timing resolution, to achieve maximum contrast for the hot lesions. The voxel size of the reconstructed images was 0.5×0.5×0.5-mm^3.

For quantitative analysis we used a contrast recovery coefficient (CRC) metric to estimate the sphere uptake accuracy for the hot spheres. For this calculation, regions-of-interest (ROIs) were drawn over the hot and cold spheres, equal in size to the sphere diameters, to obtain the mean counts (C_H for the hot, and C_C for the cold lesion). Annular regions beyond the sphere diameter of 5-mm were drawn to estimate the background counts (C_B) (inner diameter of 10-mm and outer diameter of 20-mm). The background ROIs were drawn locally in this manner due to the non-uniformities and artifacts which arise in some of the reconstructed images that will lead to incorrect estimation of the background counts. CRC for hot spheres was calculated using the NEMA definition (2001):

$$CRC=\frac{\frac{C_H}{C_B}-1}{8-1}$$

Similarly for the cold sphere, CRC was estimated by:

$$CRC=1-\frac{C_C}{C_B}$$

In addition, we also calculated a simple measure of signal-to-noise (SNR) given by:

$$SNR=\frac{\frac{C_H}{C_B}-1}{\sqrt{\left(\frac{\sigma_H}{C_H}\right)^2+\left(\frac{\sigma_B}{C_B}\right)^2}}$$

where σ_H is the standard deviation of counts in an ROI drawn over the lesion, and σ_B is the standard deviation of counts in the background ROI.

3. Results

3.1. Impact of crystal size

In Figures 2a–c we show the reconstructed images for a full ring scanner for the three crystal cross-sections investigated. Visually, it is very clear that the contrast in the three hot lesions decreases as the crystal size is increased. This is quantitatively observed in Figure 2d which shows the CRC value for the three hot lesions decreasing noticeably as the crystal cross-section is increased to 3×3-mm^2. A similar trend was observer for the cold lesion (Lesion 4) where the CRC values were 46%, 35%, and 16% for crystal cross-sections of to 1×1-mm^2, 2×2-mm^2, and 3×3-mm^2, respectively. All subsequent evaluations were performed for a scanner using 1×1×10-mm^3 crystals.

3.2. Impact of TOF on limited angle reconstruction of data from a small object

In Figure 3 we show the central transverse slice for reconstructed images for the 6-cm diameter phantom. As the angular coverage is reduced (moving from full ring through 2/3 ring to a ½ ring scanner) there is increased distortion in the image in a direction perpendicular to the detectors. With TOF information (timing resolution of 200ps), this distortion is greatly reduced.

3.3. Impact of TOF on limited angle reconstruction of data from a large object

In Figure 4 we show the central transverse slice for reconstructed images for a larger 10-cm diameter phantom. Now, as the angular coverage is reduced (moving from full ring through 2/3 ring to a ½ ring scanner) there are significant artifacts in the Non-TOF reconstructed images due to missing angular views. The TOF information still leads to more realistic reconstructed images with reduced artifacts. The two bright vertical strips in the 2/3 ring scanner Non-TOF reconstruction are due to the acceptance of LORs within the same detector at its two edges, an effect that in practice will not be present since we reject LORs with both end-points in the same detector.

3.4. Impact of TOF on CRC achieved in limited angle tomography

Figure 5 shows the measured CRC values for the three hot lesions (Lesion 1, 2, and 3) in the full, 2/3, and ½ ring scanners as function of timing resolution. The results are shown only for those images that were deemed to be relatively artifact-free for analysis. The results show that TOF imaging has no impact on the CRC values achieved in the full ring scanner. For the 2/3 ring scanner, a timing resolution of 600ps or better leads to CRC values which are similar to those achieved in the full ring scanner. The drop in CRC seen for lesion 2 in the 2/3 ring scanner with 600ps TOF reconstruction is due to bright vertical strips seen in the image due to LORs with end-points near the edges of the same detector. As a result the background estimate for this lesion is higher leading to a reduction in the CRC for that lesion. For the ½ ring scanner, on the other hand, our results indicate that a timing resolution of 300ps or better still helps achieve CRC values for all three lesions which are similar to those achieved in the full ring scanner. For a qualitative comparison, in Figure 6 we also show the central slices for the reconstructed images for the three scanner geometries as function of timing resolution. It is obvious that for the ½ ring scanner, 600ps TOF and Non-TOF images have significant artifacts, while for the 2/3 ring scanner the Non-TOF image has the most significant artifacts.

3.5. Impact of TOF on SNR achieved in a full ring scanner

In clinical whole-body imaging it has been shown that TOF imaging leads to increases in image SNR values especially as the imaging object increases in size. In breast imaging the increase in SNR, if any, is expected to be small. In Figure 7 we show the SNR values calculated for Lesions 1 and 3 in a full ring scanner as a function of scan time. Our results indicate that there is some gain in the SNR achieved for the two lesions with very good timing resolution of 200–300ps. If such high timing resolution can be achieved in a PET detector, then one can expect a basic SNR improvement with TOF information even in a full ring PET scanner.

3.6. Impact of timing resolution on SNR achieved in limited angle TOF scanners

Since limited angle tomography will also lead to a reduction in scanner sensitivity, a final step in our evaluation was to investigate the impact on SNR for limited angle scanners with TOF information. Again, our analysis was restricted to those situations that produced relatively artifact-free images. Figure 8 summarizes our results. With a timing resolution of 300ps and better, the 2/3 ring TOF scanner performs at least as well as a conventional full ring Non-TOF scanner while the ½ ring scanner requires longer scan times to achieve similar performance. With a 600ps timing resolution, a full ring TOF scanner has no noticeable advantage over a full ring Non-TOF scanner. However, with this timing resolution and slightly longer scan times, we can achieve SNR values with a 2/3 ring scanner that are similar to the full ring Non-TOF scanner.

4. Discussion and conclusions

In this work we have primarily shown the benefit of using TOF information for generating distortion or artifact-free images in a limited angle, emission tomography situation such as that encountered in dedicated breast PET imaging. In particular, without TOF information, the limited angle situation leads to not only distortions, but also severe artifacts in the reconstructed image as the object size relative to the scanner ring diameter increases. The reconstructed image in this situation for a warm cylinder with hot/cold lesions has large non-uniformities in the background. This greatly limits the use of such a PET scanner in quantitative imaging situations, especially those where the scanner ring diameter is small in order to achieve high geometric sensitivity. Consequently, detector rotation needs to be employed to cover all the missing LORs, which however leads to longer scan times or essentially a reduction in effective sensitivity.

By using TOF information, a lot of the distortions as well as non-uniform artifacts can be reduced without the need for detector rotation. However, as the angular coverage is reduced, better timing resolution is needed to produce artifact-free images. In particular, in our study we found that a timing resolution of 600ps or better was needed for a 2/3 ring scanner (scanner ring diameter of 15-cm), while a timing resolution of 300ps or better was necessary for the ½ ring scanner geometry, in order to achieve hot lesion CRC values similar to a full ring scanner. This suggests that there will eventually be a trade-off in the design of such PET scanners where the timing resolution will be determined by detector performance which, in turn, will define the minimum angular coverage needed in the scanner for artifact or distortion-free images without rotation. While this study uses a symmetric gap distribution between the two detectors, it may be possible to achieve artifact-free images with TOF PET in situations where there are more than two gaps or gaps of unequal size as well.

Since limited angle tomography leads to a reduction in sensitivity relative to a full ring scanner due to the loss of counts in the missing LORs, and we also show that there is a gain in SNR with TOF information, we calculated the relative sensitivity of various scanner geometries considered in this work relative to a full ring Non-TOF scanner. In Table I we show this sensitivity value which is simply a product of the relative geometric sensitivity (due to missing LORs) and the simple TOF gain given by Budinger (Budinger, 1983) as $D/\Delta x$, where D is the object diameter (10-cm for these calculations) and $\Delta x = c \cdot \Delta t/2$ (where c is the speed of light and Δt is the fwhm of the scanner timing resolution). The expected changes in absolute sensitivity as derived from these first principles are in reasonable agreement from the results we showed in Fig. 7 and Fig. 8 for the hot lesion SNR values. In particular the 2/3 ring scanner with 300ps timing resolution has similar performance to the full ring Non-TOF scanner.

In conclusion, we have shown that TOF PET imaging can have an important application in the design of limited angle, application specific PET scanners. By producing distortion and artifact-free images one can avoid the need for detector rotation in order to achieve quantitative, tomographic images. This can have an impact in the design of not only dedicated breast scanners, but also in-beam PET scanners for monitoring of dose delivery in proton and heavy-ion therapy machines.

Acknowledgments

We would like to thank Matthew Werner and Samuel Matej of the University of Pennsylvania for useful discussions about data processing and image reconstruction. This work was supported by the National Institutes of Health grant Nos. R01-CA113941 and R21-EB008142.

References

NEMA. Standards Publication NU 2-2001, Performance Measurements of Positron Emission Tomographs. Washington, DC: National Electrical Manufacturers Association; 2001.

Adam LE, Watson CC. Experimental determination of the lower energy discriminator level of a positron emission tomograph. Nuklearmedizin-Nuclear Medicine 1999;38:61–65. [PubMed: 10100233]

Budinger TF. Time-of-Flight Positron Emission Tomography - Status Relative to Conventional PET. J. Nucl. Med 1983;24:73–76. [PubMed: 6336778]

Conti M, Bendriem B, Casey M, Chen M, Kehren F, Michel C, Panin V. First experimental results of time-of-flight reconstruction on an LSO PET scanner. Phys. Med. Biol 2005;50:4507–4526. [PubMed: 16177486]

Doshi NK, Shao YP, Silverman RW, Cherry SR. Design and evaluation of an LSO PET detector for breast cancer imaging. Med. Phys 2000;27:1535–1543. [PubMed: 10947256]

Karp, JS.; Kuhn, A.; Perkins, AE.; Surti, S.; Werner, ME.; Daube-Witherspoon, ME.; Popescu, LM.; Vandenberghe, S.; Muehllehner, G. Characterization of TOF PET scanner based on Lanthanum Bromide. In: Seibert, JA., editor. 2005 IEEE Nuclear Science Symposium and Medical Imaging Conference. San Juan, Puerto Rico: IEEE Nuclear & Plasma Sciences Society; 2005.

Levin CS, Foudray AMK, Habte F. Impact of high energy resolution detectors on the performance of a PET system dedicated to breast cancer imaging. Physica Medica 2006;21:28–34. [PubMed: 17645990]

Moses WW, Budinger TF, Huesman RH, Derenzo SE. PET camera designs for imaging breast cancer and axillary node involvement. J. Nucl. Med 1995;36

Moses WW, Qi J. Fundamental limits of positron emission mammography. Nucl Instrum Meth A 2003;497:82–89.

Muehllehner G, Buchin MP, Dudek JH. Performance Parameters of a Positron Imaging Camera. IEEE Trans. Nucl. Sci 1976;23:528–537.

Raylman RR, Majewski S, Smith MF, Wojcik R, Weisenberger AG, Kross B, Popov V, Derakhshan JJ. Comparison of scintillators for positron emission mammography (PEM) systems. IEEE Trans. Nucl. Sci 2003;50:42–49.

Raylman RR, Majewski S, Weisenberger A, Popov V, Kross B, Wojcik R. Pixelated NaI(Tl) arrays for use in Positron Emission Mammography (PEM). J. Nucl. Med 2002;43:11p–11p.

Raylman RR, Majewski S, Weisenberger AG, Popov V, Wojcik R, Kross B, Schreiman JS, Bishop HA. Positron emission mammography-guided breast biopsy. J. Nucl. Med 2001;42:960–966. [PubMed: 11390563]

Raylman RR, Majewski S, Wojcik R, Weisenberger AG, Kross B, Popov V, Bishop HA. The potential role of positron emission mammography for detection of breast cancer. A phantom study. Med. Phys 2000;27:1943–1954. [PubMed: 10984240]

Surti S, Karp JS, Muehllehner G. Image quality assessment of LaBr3- based whole-body 3D PET scanners: a Monte Carlo evaluation. Phys. Med. Biol 2004;49:4593–4610. [PubMed: 15552419]

Surti S, Karp JS, Popescu LA, Daube-Witherspoon ME, Werner M. Investigation of time-of-flight benefit for fully 3-D PET. IEEE Trans. Med. Imag 2006;25:529–538.

Surti S, Kuhn A, Werner ME, Perkins AE, Kolthammer J, Karp JS. Performance of Philips Gemini TF PET/CT scanner with special consideration for its time-of-flight imaging capabilities. J Nucl Med 2007;48:471–480. [PubMed: 17332626]

Thompson CJ, Murthy K, Picard Y, Weinberg IN, Mako R. Positron Emission Mammography (PEM) - a Promising Technique for Detecting Breast-Cancer. IEEE Trans. Nucl. Sci 1995;42:1012–1017.

Thompson CJ, Murthy K, Weinberg IN, Mako F. Feasibility Study for Positron Emission Mammography. Med. Phys 1994;21:529–538. [PubMed: 8058019]

Townsend D, Schorr B, Jeavons A. 3-Dimensional Image-Reconstruction for a Positron Camera with Limited Angular Acceptance. IEEE Trans. Nucl. Sci 1980;27:463–470.

Vandenberghe S, Daube-Witherspoon ME, Lewitt RM, Karp JS. Fast reconstruction of 3D time-of-flight PET data by axial rebinning and transverse mashing. Phys Med Biol 2006;51:1603–1621. [PubMed: 16510966]

Vandenberghe S, Lemahieu I. System characteristics of simulated limited angle TOF PET. Nucl. Instr. Meth. (A) 2007;571:480–483.

Weinberg I, Majewski S, Weisenberger A, Markowitz A, Aloj L, Majewski L, Danforth D, Mulshine J, Cowan K, Zujewski J, Chow C, Jones E, Chang V, Berg W, Frank J. Preliminary results for positron emission mammography: Real-time functional breast imaging in a conventional mammography gantry. Eur. J. Nucl. Med 1996;23:804–806. [PubMed: 8662120]

Yang YF, Dokhale PA, Silverman RW, Shah KS, Mcclish MA, Farrell R, Entine G, Cherry SR. Depth of interaction resolution measurements for a high resolution PET detector using position sensitive avalanche photodiodes. Phys. Med. Biol 2006;51:2131–2142. [PubMed: 16625031]

Zasadny KR, Wahl RL. Standardized uptake values of normal tissues in PET with 2-[Fluorine-18]-fluoro-2-deoxy-D-glucose: variations with body weight and a method for correction. Radiol 1993;189:847–850.

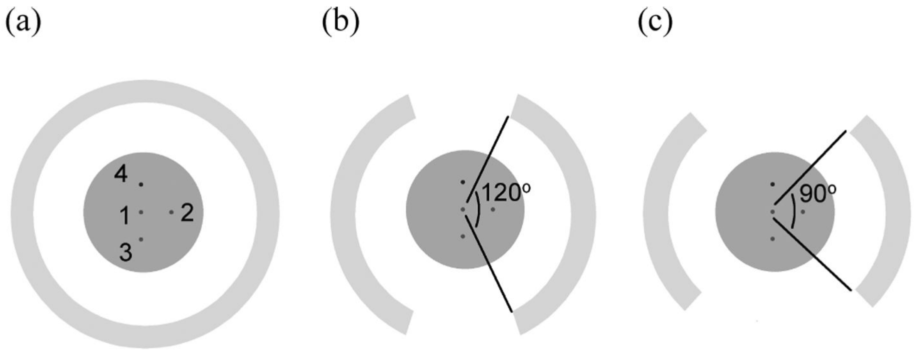

Figure 1.

Scanner setup for the (a) full, (b) 2/3 (120 degrees in-plane coverage), and (c) ½ ring (90 degrees in-plane coverage) scanners. The ring diameter and the axial length for the scanners are 15-cm. The simulated cylindrical phantom (length is 8-cm, diameter is 6 or 10-cm) has three, 5-mm diameter hot spheres (lesion 1, 2, and 3) with 8:1 uptake with respect to background, and one, 5-mm diameter cold sphere. The scanner ring diameter was fixed at 15-cm.

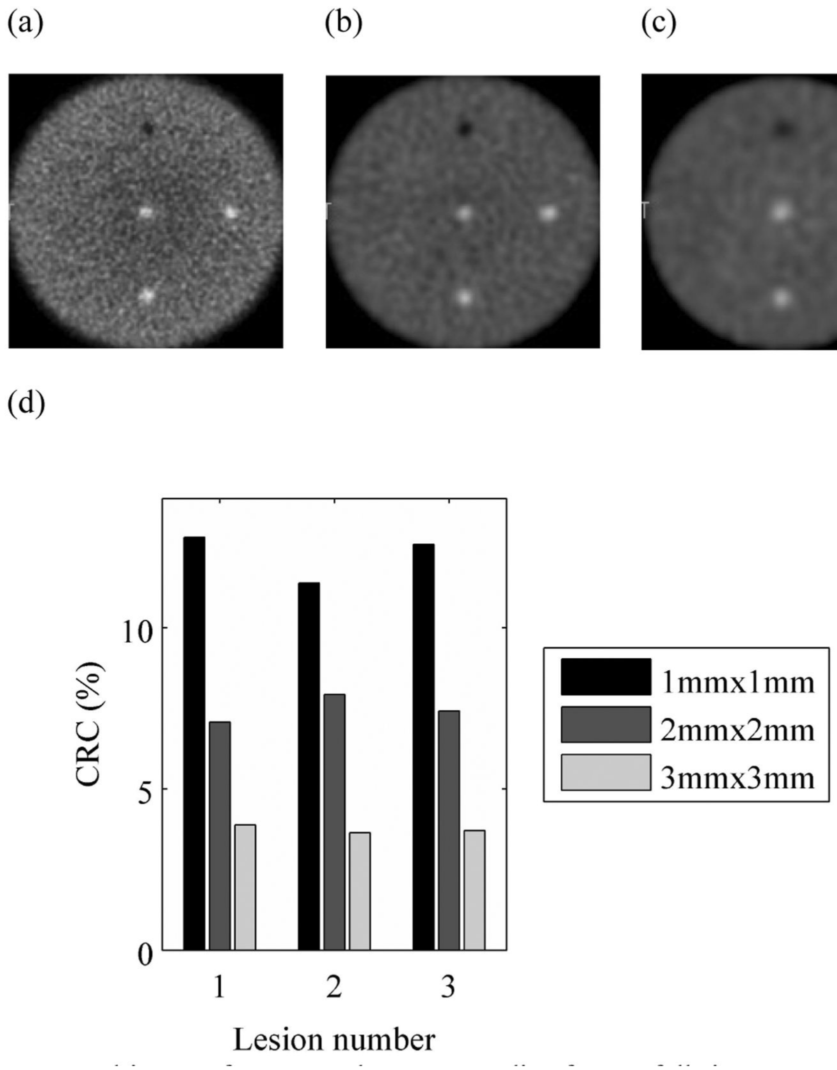

Figure 2.
Reconstructed images for a central transverse slice from a full ring scanner using three different crystal cross-sections: (a) 1×1-mm^2, (b) 2×2-mm^2, and (c) 3×3-mm^2. (d) Measured CRC values for the three hot lesions in a full ring scanner using three different crystal cross-sections, 1×1-mm^2, 2×2-mm^2, and 3×3-mm^2. The results are shown for phantom with diameter of 10-cm.

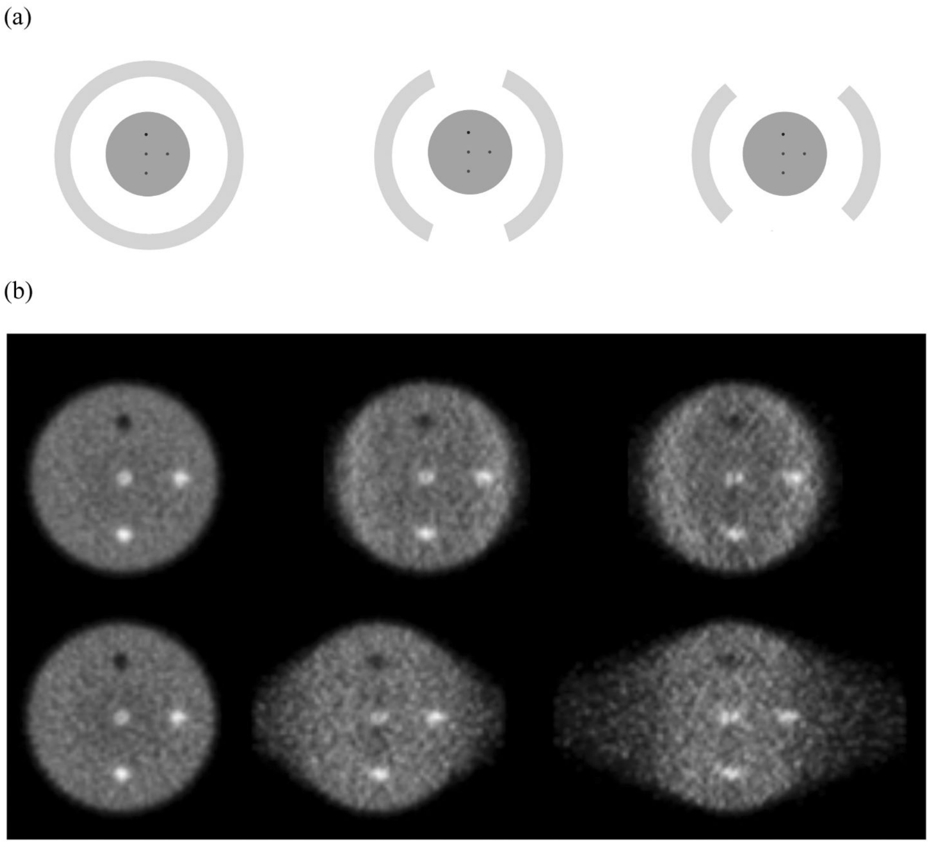

Figure 3.
(a) Schematic of detector arrangement for a full ring (Left), 2/3 ring (Middle), and ½ ring (Right) scanner. (b) Reconstructed images for a central transverse slice of a 6-cm diameter cylindrical phantom. The top row shows TOF reconstructed images (timing resolution of 200ps), while the bottom row has the Non-TOF images. The crystal size for these simulations was 1×1×10-mm^3.

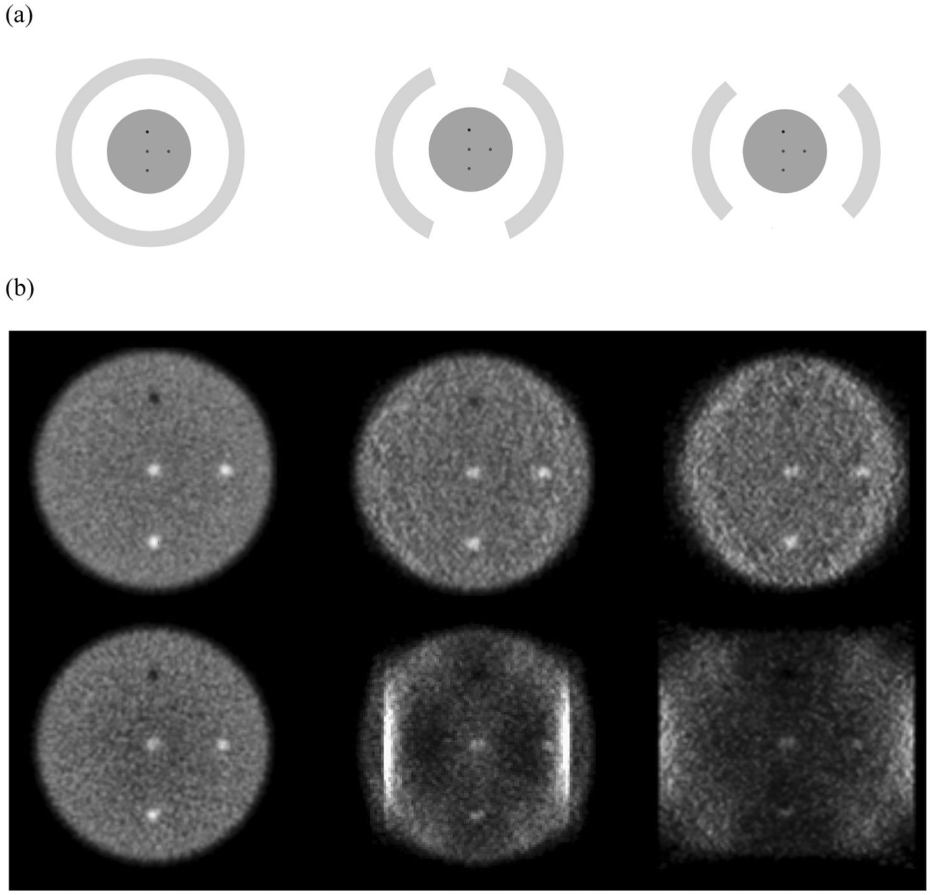

Figure 4.

(a) Schematic of detector arrangement for a full ring (Left), 2/3 ring (Middle), and ½ ring (Right) scanner. (b) Reconstructed images for a central transverse slice of a 10-cm diameter cylindrical phantom. The top row shows TOF reconstructed images (timing resolution of 200ps), while the bottom row has the Non-TOF images. The crystal size for these simulations was 1×1×10-mm^3.

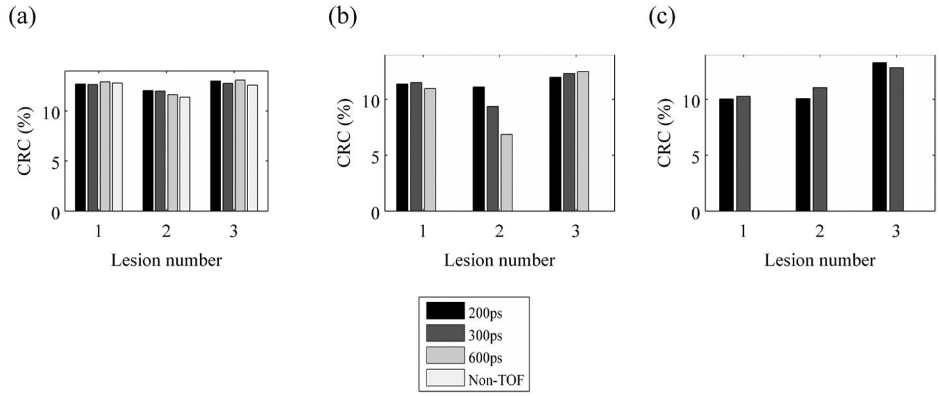

Figure 5.

CRC values for Lesions 1, 2, and 3 in a 10-cm diameter phantom for a full ring (a), 2/3 ring (b), and ½ ring (c) scanner for 200ps TOF, 300ps TOF, 600ps TOF, and Non-TOF scanners. Results are only shown for those images that were deemed relatively artifact-free. The crystal size for these simulations was 1×110-mm^3.

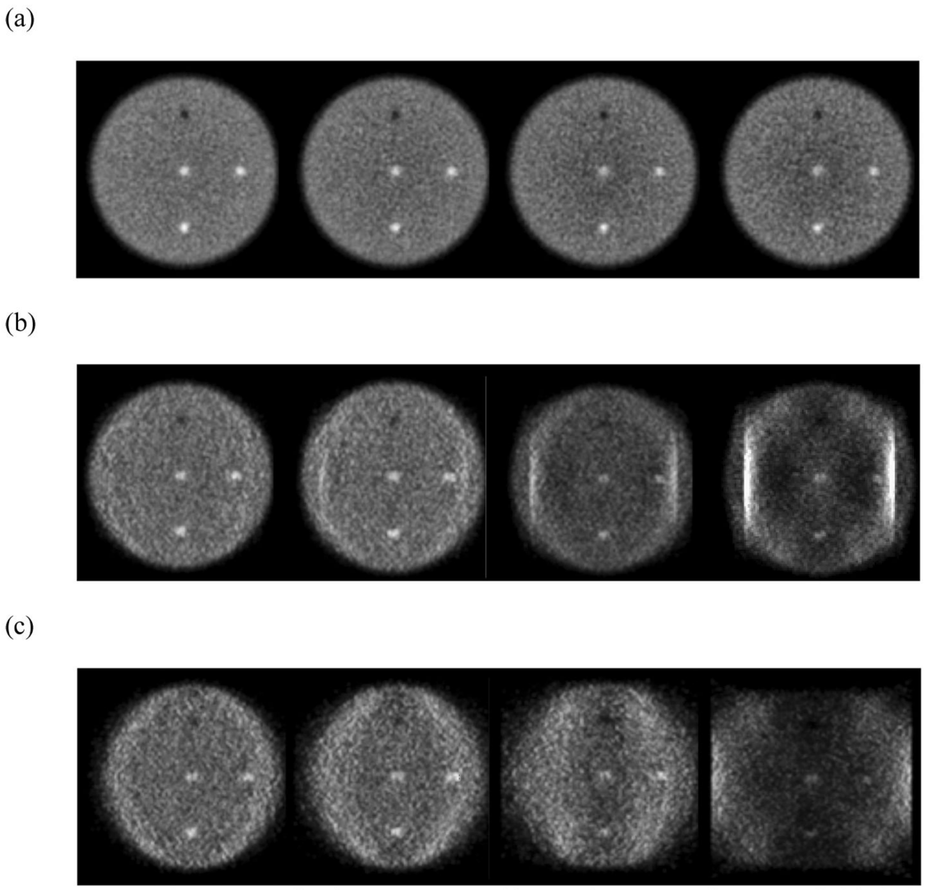

Figure 6.

Central transverse slice from reconstructed images for a 10-cm diameter cylindrical phantom in a full ring (a), 2/3 ring (b), and ½ ring (c) scanner. With each set, the four images moving left to right are: 200ps TOF, 300ps TOF, 600ps TOF, and Non-TOF. The crystal size for these simulations was 1×1×10-mm^3.

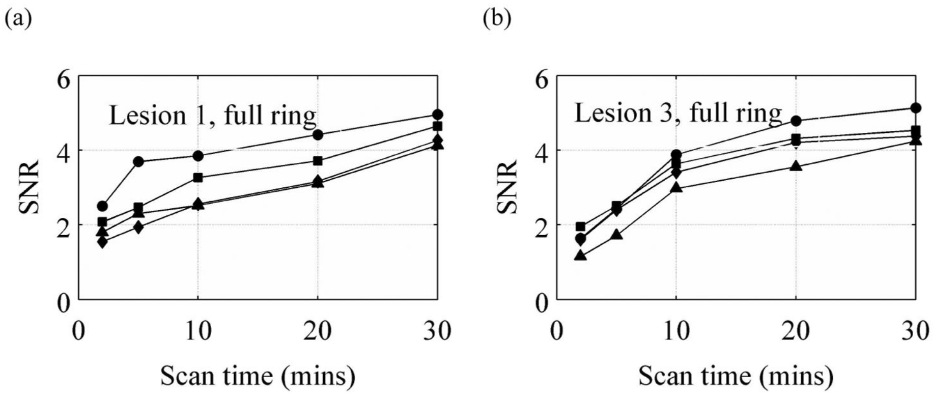

Figure 7.
SNR values for Lesions 1 (a) and 3 (b) in a 10-cm diameter phantom placed in full ring scanner with varying timing resolution. The curves with λ, ν, υ, and σ symbols are for 200ps TOF, 300ps TOF, 600ps TOF, and Non-TOF scanners, respectively. The crystal size for these simulations was 1×1×10-mm^3.

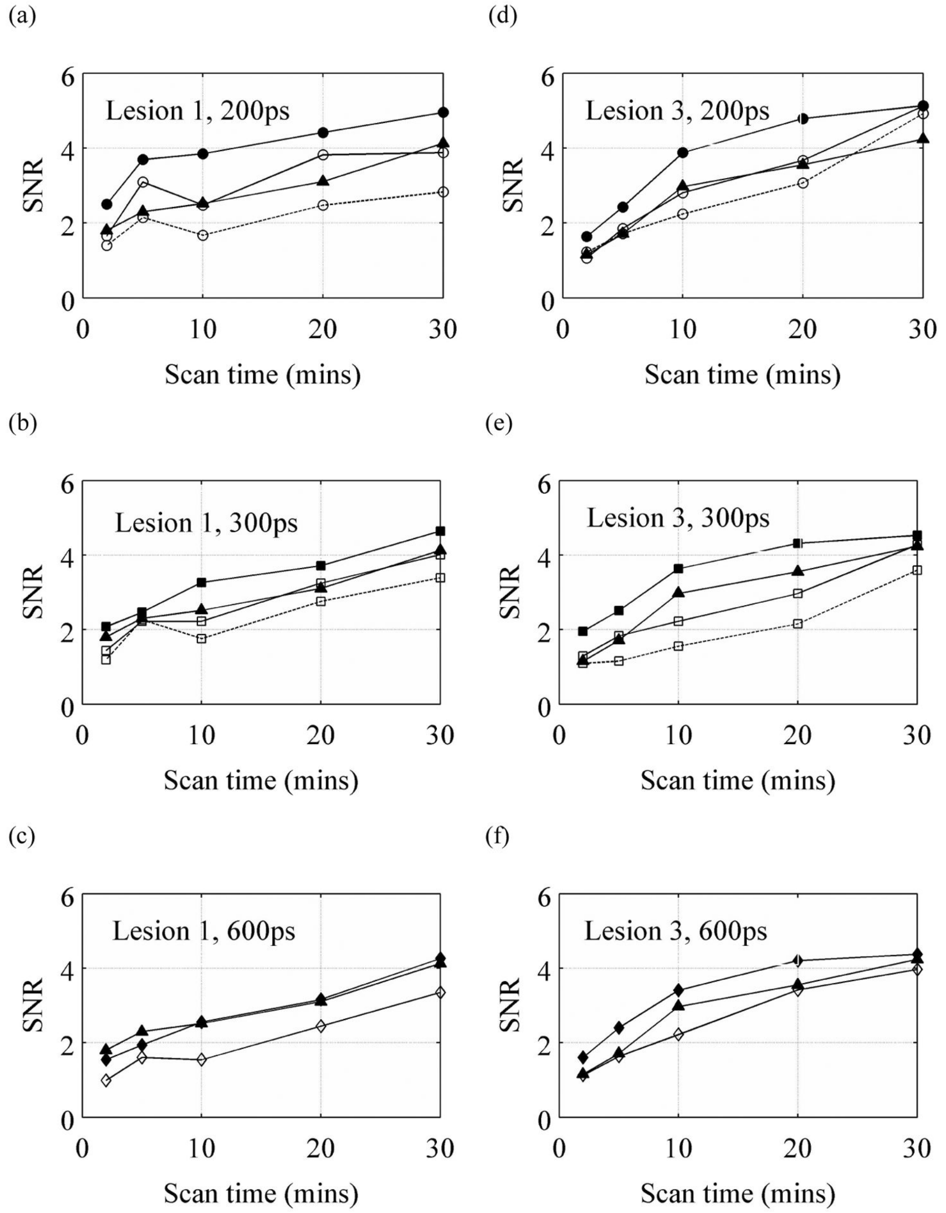

Figure 8.

SNR values vs. scan time for lesions 1 (a, b, and c) and 3 (d, e, f) for a 200ps (a and d), 300ps (b and e), and 600ps (c and f) timing resolution TOF scanner. In each plot, for comparison, the results from a full ring Non-TOF scanner are also shown with the solid line and filled σ symbol. The solid lines with filled symbols, solid lines with open symbols, and dotted lines with open symbols are for the full, 2/3, and ½ ring TOF scanners, respectively. All results are for the 10-cm diameter cylindrical phantom. Results are only shown for those images that were deemed relatively artifact-free. The crystal size for these simulations was 1×1×10-mm^3.

Table 1

Absolute sensitivity for different scanner geomtries with varying timing resolutions for TOF imaging. The geometric sensitivity is calculated for a point source placed at the center of the scanner. Numbers are relative to a full ring Non-TOF scanner.

	Timing resolution (ps)	**D/Δx**	**Relative geometric sensitivity**	**Relative absolute sensitivity**
full ring	200	3.3	1.0	3.3
	300	2.2	1.0	2.2
	600	1.1	1.0	1.1
2/3 ring	200	3.3	0.44	1.5
	300	2.2	0.44	1.0
	600	1.1	0.44	0.5
½ ring	200	3.3	0.25	0.8
	300	2.2	0.25	0.6